Sensorless Control of Synchronous Reluctance Motor Drives: Improved Modeling and Analysis Beyond Active Flux

Sensorless Control of Synchronous Reluctance Motor Drives: Improved Modeling and Analysis beyond Active Flux

Anantaram Varatharajan
Department of Energy
Politecnico di Torino
Torino, Italy
anantaram.varatharajan@polito.it

Gianmario Pellegrino
Department of Energy
Politecnico di Torino
Torino, Italy
gianmario.pellegrino@polito.it

***Abstract*—The paper presents a framework for the design and analysis of position observers for sensorless control of synchronous reluctance machines. An improved inductance model is developed to account for the position error induced inductance variations. The instability regions of active flux based position observer are analytically identified and validated. A novel technique, Adaptive Projection vector for Position error estimation (APP), that alleviates the stability problems is introduced. Furthermore, the proposed technique can be augmented with a second projection vector to estimate speed error independently of the position error, referred to as Adaptive Projection vector matrix for Position and Speed error estimation (APPS). Stability and performance of proposed technique is validated on a 1 kW synchronous reluctance motor test bench.**

***Index Terms*—Sensorless control, active flux, synchronous reluctance machine, speed error estimation, stability analysis.**

I. Introduction

Owing to the saliency of synchronous reluctance (SyR) machine, the position and speed estimation without an encoder or resolver becomes realizable. The fundamental wave excitation based approach is usually adopted at medium and high speeds regions. For zero to low speeds operation, the literature contains numerous works on high frequency signal injection [1] [2] and switching frequency excitation [3] methods; [4] presents a comprehensive review of high frequency injection techniques. Fusion methods for smooth transitioning between the two models are reported in [5] [6].

The present work concerns with the fundamental wave excitation approach although it can be augmented with the high frequency injection scheme with ease. Multiple works report on the established active flux based sensorless control for medium-high speeds region [5] [6] [7]. Yet, a comprehensive stability analysis of the active flux approach has been largely open. A generic observer framework for analysis is developed in [8] with the concept of projection vectors to derive the position error signal that drives a phase locked loop (PLL) or a speed adaptation law. Instability of active flux approach in the form of one among the many possible projection vectors is studied for high speed regions in [8].

The section II introduces the machine model, control system notations and the position observer in the form of a PLL. The main contributions of the paper are summarized as follows:

- A generic framework for stability analysis, along the lines of [8], with an improved inductance modeling is developed in section II. Contrary to convention, the improved inductance model also accounts for the position error induced variations.
- The active flux based approach is subjected to analysis to reveal the regions of instability in section III.
- A new position observer, Adaptive Projection vector for Position error estimation (APP), is developed and analyzed for stability in section IV.
- The proposed technique is shown to have the capability to estimate speed error in addition to and independent of the position error with a second projection vector, named Adaptive Projection vector matrix for Position and Speed error estimation (APPS).

The section V presents the experimental evaluation on the instability of active flux method, the steady-state and transient performance of the proposed technique along with the speed error estimation on a 1 kW SyR motor test bench.

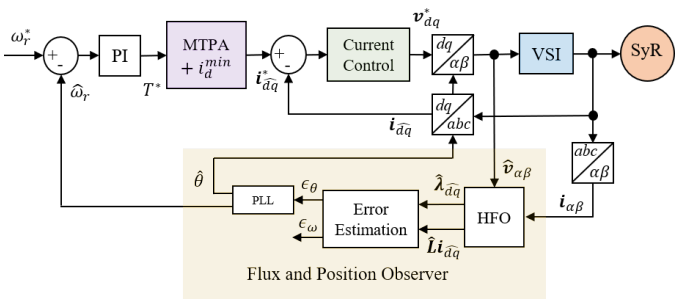

Fig. 1. Control system block diagram depicting position observer aided by Hybrid Flux Observer (HFO). Current vector control can be replaced by any other scheme.

II. Sensorless Control System

The electrical rotor position is θ and the electrical angular speed is $\omega = s\,\theta$. Estimated vectors are represented by the superscript $\hat{}$. The orthogonal rotational matrix is $\mathbf{J} = \left[\begin{smallmatrix} 0 & -1 \\ 1 & 0 \end{smallmatrix}\right]$ and $\mathbf{I}$ is the identity matrix.

The machine model is expressed in coordinates of estimated rotor reference frame, denoted by subscript $\hat{dq}$, whose d-axis is at $\hat{\theta} = \theta - \tilde{\theta}$, where $\tilde{\theta}$ is the position error. The speed error is symbolized by $\tilde{\omega} = \omega - \hat{\omega}$. Real space vectors will be used; for example, the stator current is $\boldsymbol{i}_{\hat{dq}} = [i_{\hat{d}}, i_{\hat{q}}]^{\mathrm{T}}$ where $i_{\hat{d}}$ and $i_{\hat{q}}$ are the vector components in estimated rotor reference frame. Space vectors in stationary reference frame are denoted by subscript $\alpha\beta$.

The block diagram illustrating an overview of the motor control is shown in the Fig. 1.

A. Mathematical Model of SyR Machine

The voltage equation of a SyR machine is expressed in (1) where R_s is the stator resistance and $\boldsymbol{\lambda}_{\hat{dq}}$ is the stator flux linkage.

$$s\,\boldsymbol{\lambda}_{\hat{dq}} = \boldsymbol{v}_{\hat{dq}} - R_s \boldsymbol{i}_{\hat{dq}} - \hat{\omega}\,\mathbf{J}\,\boldsymbol{\lambda}_{\hat{dq}} \tag{1}$$

The stator flux linkage and its time-derivative in terms of the incremental inductance $\boldsymbol{l}$ and apparent inductance $\boldsymbol{L}$ matrices are expressed in (2).

$$\boldsymbol{\lambda}_{\hat{dq}} = \mathrm{e}^{\mathbf{J}\tilde{\theta}}\,\boldsymbol{L}\,\mathrm{e}^{-\mathbf{J}\tilde{\theta}}\,\boldsymbol{i}_{\hat{dq}} \tag{2a}$$

$$s\,\boldsymbol{\lambda}_{\hat{dq}} = (s\,\tilde{\theta})\,\mathbf{J}\,\boldsymbol{\lambda}_{\hat{dq}} + \mathrm{e}^{\mathbf{J}\tilde{\theta}}\,\boldsymbol{l}\,s\left(\mathrm{e}^{-\mathbf{J}\tilde{\theta}}\,\boldsymbol{i}_{\hat{dq}}\right) \tag{2b}$$

The components of inductance matrices are shown in (3) where l_d, l_q represents the incremental inductance along direct d and quadrature q axis respectively while l_{dq} is the cross-saturation term. Apparent inductance are defined likewise. All quantities are a function of $\boldsymbol{i}_{dq}$.

$$\boldsymbol{l}(\boldsymbol{i}_{dq}) = \begin{bmatrix} l_d & l_{dq} \\ l_{dq} & l_q \end{bmatrix} \qquad \boldsymbol{L}(\boldsymbol{i}_{dq}) = \begin{bmatrix} L_d & 0 \\ 0 & L_q \end{bmatrix} \tag{3}$$

The estimated electromagnetic torque is given by (4) where p is the number of pole pairs.

$$\hat{T} = \frac{3p}{2}(\boldsymbol{\lambda}_{\hat{dq}} \times \boldsymbol{i}_{\hat{dq}}) \tag{4}$$

B. State Observer

The flux observer is implemented in stator reference frame as defined by (5) where $\boldsymbol{G}_{\alpha\beta}$ is a 2×2 gain matrix.

$$s\hat{\boldsymbol{\lambda}}_{\alpha\beta} = \hat{\boldsymbol{v}}_{\alpha\beta} - R_s \boldsymbol{i}_{\alpha\beta} + \boldsymbol{G}_{\alpha\beta}\left(\mathrm{e}^{\mathbf{J}\hat{\theta}}\,\hat{\boldsymbol{L}}\,\mathrm{e}^{-\mathbf{J}\hat{\theta}}\boldsymbol{i}_{\alpha\beta} - \hat{\boldsymbol{\lambda}}_{\alpha\beta}\right) \tag{5}$$

$\hat{\boldsymbol{L}}$ is the apparent inductance from the current model in estimated rotor reference frame. In principle, the term $\hat{\boldsymbol{L}}$ comprises of two different types of errors: inherent parameter error in inductance, and position error induced inductance error in sensorless control.

Let $\boldsymbol{\Lambda}$ denote the flux maps lookup table of the machine under test as $\boldsymbol{\lambda}_{dq} = \boldsymbol{\Lambda}(\boldsymbol{i}_{dq})$, shown in the Fig. 2. Parameter errors are not considered in this work, i.e., $\hat{\boldsymbol{\Lambda}} = \boldsymbol{\Lambda}$ is assumed. Then, in the estimated reference frame, the current model

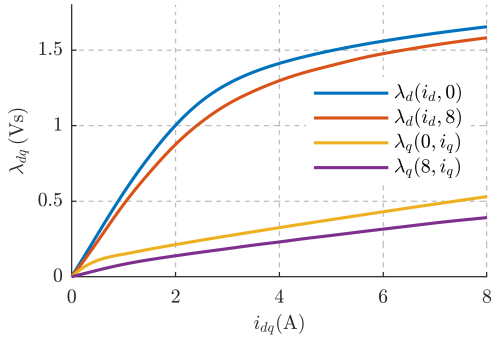

Fig. 2. Experimentally obtained flux maps lookup table, $\boldsymbol{\Lambda}$, of the SyR motor under test: $\boldsymbol{\lambda}_{dq} = \boldsymbol{\Lambda}(\boldsymbol{i}_{dq}) = \boldsymbol{L} \cdot \boldsymbol{i}_{dq}$

based inductance $\hat{\boldsymbol{L}}$ depends on the operating point $\boldsymbol{i}_{\hat{dq}}$ as in (6) whereas the real machine inductance $\boldsymbol{L}$ depends on $\boldsymbol{i}_{dq}$ as in (7).

$$\hat{\boldsymbol{L}}(\boldsymbol{i}_{\hat{dq}}) \cdot \boldsymbol{i}_{\hat{dq}} = \boldsymbol{\Lambda}(\boldsymbol{i}_{\hat{dq}}) \tag{6}$$

$$\boldsymbol{L}(\boldsymbol{i}_{dq}) \cdot \mathrm{e}^{-\mathbf{J}\tilde{\theta}}\,\boldsymbol{i}_{\hat{dq}} = \boldsymbol{\Lambda}(\mathrm{e}^{-\mathbf{J}\tilde{\theta}}\,\boldsymbol{i}_{\hat{dq}}) \tag{7}$$

Note that the components of $\hat{\boldsymbol{L}}$ are also denoted by the superscript $\hat{}$. It is worth pointing out that in case of linear flux maps (i.e. constant L_d and L_q), the inductance operator becomes invariant to position error, $\hat{\boldsymbol{L}} = \boldsymbol{L}$.

In the estimated rotor reference frame, state observer takes the form in (8) where the gain matrix $\boldsymbol{G}$ equivalence is given by (9).

$$s\,\hat{\boldsymbol{\lambda}}_{\hat{dq}} = \hat{\boldsymbol{v}}_{\hat{dq}} - R_s \boldsymbol{i}_{\hat{dq}} - \hat{\omega}\mathbf{J}\,\hat{\boldsymbol{\lambda}}_{\hat{dq}} + \boldsymbol{G}\left(\hat{\boldsymbol{L}}\,\boldsymbol{i}_{\hat{dq}} - \hat{\boldsymbol{\lambda}}_{\hat{dq}}\right) \tag{8}$$

$$\boldsymbol{G} = \mathrm{e}^{-\mathbf{J}\hat{\theta}}\,\boldsymbol{G}_{\alpha\beta}\,\mathrm{e}^{\mathbf{J}\hat{\theta}} \tag{9}$$

C. Speed and Position Observer

A conventional PLL with a proportional-integral (PI) controller is employed to drive the error signal ϵ_θ to zero as in (10) where k_p and k_i are the respective gains.

$$\hat{\omega} = k_p\,\epsilon_\theta + \int k_i\,\epsilon_\theta\,\mathrm{d}t \qquad \hat{\theta} = \int \hat{\omega}\,\mathrm{d}t \tag{10}$$

The generalized error signal [8] is defined as the projection of the difference in observed and current model flux estimates on a projection vector $\boldsymbol{\phi}_\theta$.

$$\epsilon_\theta = \boldsymbol{\phi}_\theta^{\mathrm{T}}\,(\hat{\boldsymbol{\lambda}}_{\hat{dq}} - \hat{\boldsymbol{L}}\,\boldsymbol{i}_{\hat{dq}}) \tag{11}$$

The selection of projection vector plays a crucial role in stability as discussed in the succeeding section.

D. Linearized Error Dynamics

The operating point quantities are signified by a subscript 0 and accurate model parameters in stator resistance and inductances are assumed. The flux error dynamics (12) is derived from (8) where $\tilde{\boldsymbol{\lambda}}_{\hat{dq}} = \boldsymbol{\lambda}_{\hat{dq}} - \hat{\boldsymbol{\lambda}}_{\hat{dq}}$.

$$s\,\tilde{\boldsymbol{\lambda}}_{\hat{dq}} = -(\boldsymbol{G}_0 + \omega_0\mathbf{J})\,\tilde{\boldsymbol{\lambda}}_{\hat{dq}} + \boldsymbol{G}_0\,(\boldsymbol{\lambda}_{\hat{dq}0} - \hat{\boldsymbol{L}}\,\boldsymbol{i}_{\hat{dq}0}) \tag{12}$$

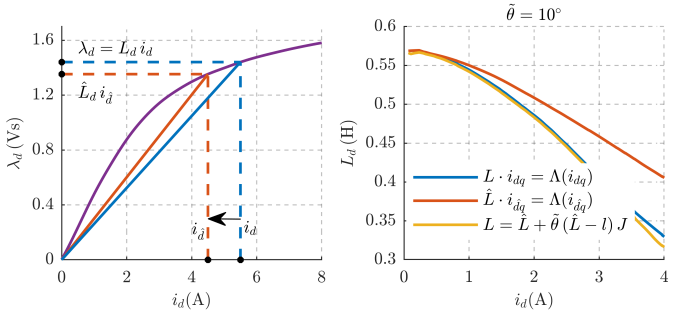

Fig. 3. Apparent inductance variation due to position error in d axis: a) In blue are the current i_d and flux $\lambda_d = L_d\, i_d$ while in red are the corresponding quantities, $i_{\hat{d}}$ and $\lambda^i_{\hat{d}} = \hat{L}_d\, i_{\hat{d}}$, in the estimated reference frame for a positive position error; b) Real machine d axis inductance (blue), current model estimate (red) and improved model (yellow) for a position error of $\tilde{\theta} = 10°$ on MTPA trajectory.

Examining the terms,

$$\boldsymbol{\lambda}_{\hat{d}q0} - \hat{\boldsymbol{L}}\, \boldsymbol{i}_{\hat{d}q0} = (\boldsymbol{L} - \hat{\boldsymbol{L}})\, \boldsymbol{i}_{\hat{d}q0} + \tilde{\theta}\, (\mathbf{J}\, \boldsymbol{L} - \boldsymbol{L}\, \mathbf{J})\, \boldsymbol{i}_{\hat{d}q0} \tag{13}$$

In literature, it is common to assume the estimated apparent inductance to be equal to the real machine inductance, $\hat{\boldsymbol{L}} \approx \boldsymbol{L}$, for small $\tilde{\theta}$ which is not always acceptable, as shown in the following.

E. Improved Inductance Model

While the approximation $\hat{\boldsymbol{L}} \approx \boldsymbol{L}$ stands for linear unsaturated regions, it is more reasonable to consider invariance in incremental rather than apparent inductance within a close vicinity, as illustrated in the Fig. 3.a. Thus, linearizing (7) gives

$$\begin{aligned} \boldsymbol{L} \cdot (\boldsymbol{i}_{\hat{d}q0} - \tilde{\theta}\mathbf{J}\, \boldsymbol{i}_{\hat{d}q0}) &= \boldsymbol{\Lambda}(\boldsymbol{i}_{\hat{d}q0} - \tilde{\theta}\, \mathbf{J}\, \boldsymbol{i}_{\hat{d}q0}) \\ &\approx \boldsymbol{\Lambda}(\boldsymbol{i}_{\hat{d}q0}) - \tilde{\theta}\, \boldsymbol{l}\, \mathbf{J}\, \boldsymbol{i}_{\hat{d}q0} \end{aligned} \tag{14}$$

On simplification using (6),

$$\boldsymbol{L} \approx \hat{\boldsymbol{L}} + \tilde{\theta}\, (\hat{\boldsymbol{L}} - \boldsymbol{l})\, \mathbf{J} \tag{15}$$

Fig. 3.b shows the real machine inductance (7), current model estimate (6) and the improved model (15) for a position error of $\tilde{\theta} = 10°$ on MTPA trajectory; it is seen that the improved model is identical to the real inductance whereas the conventional model diverges as the d axis saturates.

Using the improved inductance model (15) in (13),

$$\boldsymbol{\lambda}_{\hat{d}q0} - \hat{\boldsymbol{L}}\, \boldsymbol{i}_{\hat{d}q0} \approx \tilde{\theta}\, (\mathbf{J}\, \hat{\boldsymbol{L}} - \boldsymbol{l}\, \mathbf{J})\, \boldsymbol{i}_{\hat{d}q0} \tag{16}$$

Let $\boldsymbol{\lambda}^a_{\hat{d}q0}$ be the co-efficient of $\tilde{\theta}$ in (16), referred as auxiliary flux linkage vector in [8].

$$\boldsymbol{\lambda}^a_{\hat{d}q0} = \left(\mathbf{J}\, \hat{\boldsymbol{L}} - \boldsymbol{l}\, \mathbf{J}\right) \boldsymbol{i}_{\hat{d}q0} = \begin{bmatrix} (l_d - \hat{L}_q)\, i_{\hat{q}0} - l_{dq}\, i_{\hat{d}0} \\ (\hat{L}_d - l_q)\, i_{\hat{d}0} + l_{dq}\, i_{\hat{q}0} \end{bmatrix} \tag{17}$$

The equivalent expression for the conventional inductance model, $\hat{\boldsymbol{L}} = \boldsymbol{L}$, is (18), denoted as $\boldsymbol{\lambda}^{a'}_{\hat{d}q0}$.

$$\boldsymbol{\lambda}^{a'}_{\hat{d}q0} = \left(\mathbf{J}\, \hat{\boldsymbol{L}} - \hat{\boldsymbol{L}}\, \mathbf{J}\right) \boldsymbol{i}_{\hat{d}q0} = (\hat{L}_d - \hat{L}_q) \begin{bmatrix} i_{\hat{q}0} \\ i_{\hat{d}0} \end{bmatrix} \tag{18}$$

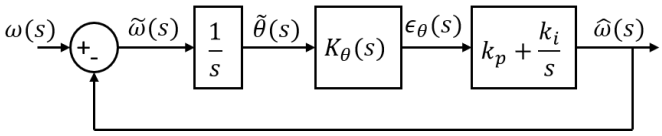

Fig. 4. Analysis of closed loop transfer function of speed observer

It is worth mentioning that, at deep saturation of d axis, the term $l_d - \hat{L}_q$ diminishes and could possibly even become negative. Hence, care must be taken to refrain from relying on $\lambda^a_{\hat{d}0}$ for position error estimation. On the other hand, this phenomenon is invisible in $\lambda^{a'}_{\hat{d}0}$, which signifies the importance of improved inductance modeling.

F. Closed Loop Transfer Function of Speed Observer

Using the improved inductance model, the error dynamics of the system simplifies to

$$s\, \tilde{\boldsymbol{\lambda}}_{\hat{d}q} = -(\boldsymbol{G}_0 + \omega_0 \mathbf{J})\, \tilde{\boldsymbol{\lambda}}_{\hat{d}q} + \tilde{\theta}\, \boldsymbol{G}_0\, \boldsymbol{\lambda}^a_{\hat{d}q0} \tag{19}$$

$$\epsilon_{\theta 0} = \boldsymbol{\phi}^{\mathrm{T}}_{\theta 0} \left(\boldsymbol{\lambda}^a_{\hat{d}q0}\, \tilde{\theta} - \tilde{\boldsymbol{\lambda}}_{\hat{d}q}\right) \tag{20}$$

The transfer function $K_\theta(s)$ from position error $\tilde{\theta}(s)$ to the error signal $\epsilon_\theta(s)$ in Fig. 4 is given by (21) .

$$K_{\theta 0} = \frac{\epsilon_{\theta 0}}{\tilde{\theta}} = \boldsymbol{\phi}^{\mathrm{T}}_{\theta 0}\, (s\, \mathbf{I} + \boldsymbol{G}_0 + \omega_0 \mathbf{J})^{-1}\, (s\, \mathbf{I} + \omega_0 \mathbf{J})\, \tilde{\boldsymbol{\lambda}}_{\hat{d}q0} \tag{21}$$

Finally, the closed loop transfer function of speed observer for the PLL in (10) is given by

$$\frac{\hat{\omega}(s)}{\omega(s)} = \frac{(s k_p + k_i)\, K_{\theta 0}(s)}{s^2 + (s k_p + k_i)\, K_{\theta 0}(s)} \tag{22}$$

III. Active Flux Based Position Estimation

The error signal $\epsilon_{\theta 0}$ in the active flux based sensorless control is proportional to the q axis component of $\boldsymbol{\lambda}^{af}_{\hat{d}q}$ in (23).

$$\boldsymbol{\lambda}^{af}_{\hat{d}q} = \hat{\boldsymbol{\lambda}}_{\hat{d}q} - \hat{L}_q\, \boldsymbol{i}_{\hat{d}q} \tag{23}$$

In accordance with former definitions, projection vector for active flux based error signal is given by (24).

$$\boldsymbol{\phi}^{af}_{\theta 0} = \frac{1}{(\hat{L}_d - \hat{L}_q)\, i_{\hat{d}0}} \begin{bmatrix} 0 \\ 1 \end{bmatrix} \tag{24}$$

Considering $\boldsymbol{G} = g\, \mathbf{I}$, the transfer function $K_{\theta 0}$ in (21) simplifies to

$$K_{\theta 0}(s) = \frac{1}{(\hat{L}_d - \hat{L}_q)\, i_{\hat{d}0}} \cdot \frac{\omega_0\, g\, \lambda^a_{\hat{d}0} + (s^2 + s g + \omega_0^2)\, \lambda^a_{\hat{q}0}}{(s + g)^2 + \omega_0^2} \tag{25}$$

It can be discerned that the steady-state terms $\omega_0\, g\, \lambda^a_{\hat{d}0} + \omega_0^2\, \lambda^a_{\hat{q}0}$ in the numerator of (25) are not additive during braking which could potentially lead to instability.

To sketch regions of instability in dq current plane, a comprehensive search is carried out by calculating the poles of speed observer transfer function (22) at all permissible optimal operating states, respecting MTPA, MTPV and current limits as shown in Fig. 5. Evaluated with conventional inductance

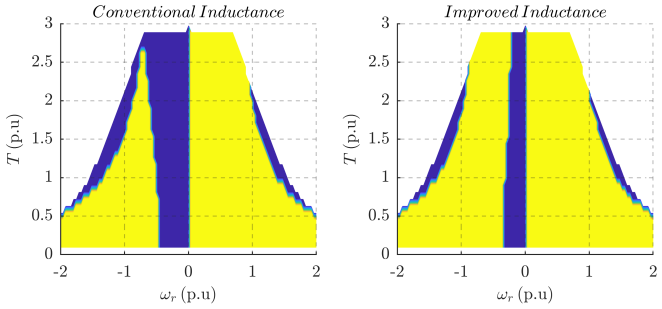

Fig. 5. Stable operating limits contour for active flux projection vector ϕ_{af} respecting MTPA, current and voltage constraints at $g = 2\pi \cdot 20$ rad/s: a) Conventional inductance model; b) Improved inductance model. Maximum current is set to 1.5 p.u. The gains of PLL are tuned according to (34) with $\Omega_\omega = 2\,\pi \cdot 25$ rad/s.

model, i.e., using $\boldsymbol{\lambda}^{a'}_{\hat{d}q0}$ in the place of $\boldsymbol{\lambda}^{a}_{\hat{d}q0}$ in (25), the results in Fig. 5.a are more conservative, an over-estimation of instability regions w.r.t the improved model in Fig. 5.b.

To alleviate the aforementioned problems, [8] proposes an adaptive gain matrix such that $\boldsymbol{G}\,\tilde{\boldsymbol{\lambda}}_{\hat{d}q0} = 0$ to decouple the dynamics of flux and the speed observer.

IV. Proposed Sensorless Technique

A. Adaptive Projection Vector for Position Error Estimation - APP

A primary design consideration for the proposed technique is to circumvent the stability issues due to the interaction of flux and speed observer dynamics; this is achieved by adapting the projection vector $\boldsymbol{\phi}_\theta$ while keeping the observer gain matrix constant, $\boldsymbol{G} = g\,\mathbf{I}$, in contrast to [8]. To this end, using the flux error dynamics (19), the error function (20) is manipulated to

$$\begin{aligned}\epsilon_{\theta 0} &= \boldsymbol{\phi}^{\mathrm{T}}_{\theta 0}\,(s\,\mathbf{I} + \boldsymbol{G}_0 + \omega_0\mathbf{J})^{-1}\,(s\,\mathbf{I} + \omega_0\mathbf{J})\,\boldsymbol{\lambda}^{a}_{\hat{d}q0}\,\tilde{\theta}\\ &= \boldsymbol{\phi}^{\mathrm{T}}_{\theta 0}\,(s\,\mathbf{I} + \boldsymbol{G}_0 + \omega_0\mathbf{J})^{-1}\,(\lambda^{a}_{\hat{d}0}\,\mathbf{I} + \lambda^{a}_{\hat{q}0}\mathbf{J})\begin{bmatrix} s\,\tilde{\theta}\\ \omega_0\,\tilde{\theta}\end{bmatrix}\end{aligned} \tag{26}$$

Examining the expression in (26), a natural choice for the position error projection vector $\boldsymbol{\phi}_{\theta 0}$ is

$$\boldsymbol{\phi}^{\mathrm{T}}_{\theta 0} = \begin{bmatrix}0 & \omega_0^{-1}\end{bmatrix}\,\left(\lambda^{a}_{\hat{d}0}\,\mathbf{I} + \lambda^{a}_{\hat{q}0}\,\mathbf{J}\right)^{-1}\left(s\,\mathbf{I} + \boldsymbol{G}_0 + \omega_0\,\mathbf{J}\right) \tag{27}$$

To address the derivate term in the projection vector, an observer is designed with a bandwidth h rad/s as shown in the block diagram in Fig. 6. Hence, the projection vector transforms to

$$\boldsymbol{\phi}^{\mathrm{T}}_{\theta 0} = \begin{bmatrix}0 & \omega_0^{-1}\end{bmatrix}\,\left(\lambda^{a}_{\hat{d}0}\,\mathbf{I} + \lambda^{a}_{\hat{q}0}\,\mathbf{J}\right)^{-1}\left(\frac{sh}{s+h}\,\mathbf{I} + \boldsymbol{G}_0 + \omega_0\,\mathbf{J}\right) \tag{28}$$

For $\boldsymbol{G} = g\,\mathbf{I}$, the transfer function $K_{\theta 0}$ in (21) reduces to

$$K_{\theta 0} = \frac{s^2 + g^2 + \omega_0^2 + s\,g + g\,s\left(\frac{h}{s+h}\right)}{(s+g)^2 + \omega_0^2} \tag{29}$$

It is discerned that the $K_{\theta 0}$ is independent of $\boldsymbol{\lambda}^{a}_{\hat{d}q}$, $\boldsymbol{i}_{\hat{d}q}$ and the sign of ω. Moreover, as $h \to \infty$, $K_{\theta 0} \to 1$; however, h is limited by the high frequency noise.

The bode plot at various speeds is shown in the Fig. 7, with/without the derivative observer; it imitates a band-stop filter with notch frequency of ω and the derivative observer is seen to not have a major impact on $K_{\theta 0}$.

The locus of poles for the close loop transfer function of speed observer (22) is shown in the Fig. 8 and is observed to be stable in all operating points. Although succeeding analysis and results correspond to $\boldsymbol{G} = g\,\mathbf{I}$, it is worth pointing out that the gain matrix can be adapted as in (30) at $h = 0$ to obtain $K_{\theta 0} = 1$ that results in fixed PLL poles and the complex poles of flux observer at $s = -g \pm j\,\omega$.

$$\boldsymbol{G}_0 = \frac{g^2\,\mathbf{I} - 2g\,\omega_0\,\mathbf{J}}{\omega_0\,|\boldsymbol{\lambda}^{a}_{\hat{d}q0}|^2}\begin{bmatrix}\lambda^{a}_{\hat{d}0}\lambda^{a}_{\hat{q}0} & -\lambda^{a\;2}_{\hat{d}0}\\ \lambda^{a\;2}_{\hat{q}0} & -\lambda^{a}_{\hat{d}0}\lambda^{a}_{\hat{q}0}\end{bmatrix} \tag{30}$$

B. Adaptive Projection Vector Matrix for Position and Speed Error Estimation - APPS

For the speed observer structure defined in (10), the derivative of position error is equivalent to the speed error, $s\tilde{\theta} = \tilde{\omega}$. Note that the equivalence does not hold for a PID-type mechanical observer [9].

The speed error is estimated from the expression in (26); though it is not employed in the PLL at present, it is valuable in designing high performance observers. The cumulative error signal vector $\boldsymbol{\epsilon}$ is given by (31) where the projection vector matrix (2×2) is $\boldsymbol{\Phi} = [\boldsymbol{\phi}_\omega \quad \boldsymbol{\phi}_\theta]$

$$\begin{aligned}\boldsymbol{\epsilon} = \begin{bmatrix}\epsilon_\omega\\ \epsilon_\theta\end{bmatrix} &= \boldsymbol{\Phi}^{\mathrm{T}}\,(\hat{\boldsymbol{\lambda}}_{\hat{d}q} - \hat{\boldsymbol{L}}\,\boldsymbol{i}_{\hat{d}q})\\ &= \begin{bmatrix}\boldsymbol{\phi}^{\mathrm{T}}_{\omega}\\ \boldsymbol{\phi}^{\mathrm{T}}_{\theta}\end{bmatrix}\,(\hat{\boldsymbol{\lambda}}_{\hat{d}q} - \hat{\boldsymbol{L}}\,\boldsymbol{i}_{\hat{d}q})\end{aligned} \tag{31}$$

The projection vector matrix is derived akin to (28) as

$$\boldsymbol{\Phi}^{\mathrm{T}}_0 = \begin{bmatrix}1 & 0\\ 0 & \omega_0^{-1}\end{bmatrix}\,\left(\lambda^{a}_{\hat{d}0}\,\mathbf{I} + \lambda^{a}_{\hat{q}0}\,\mathbf{J}\right)^{-1}\left(\frac{sh}{s+h}\,\mathbf{I} + \boldsymbol{G}_0 + \omega_0\,\mathbf{J}\right) \tag{32}$$

For $\boldsymbol{G} = g\,\mathbf{I}$, the transfer function $K_\omega(s)$ from speed error $\tilde{\omega}(s)$ to the error signal $\epsilon_\omega(s)$ is expressed in (33). Similar to $K_{\theta 0}$, it is independent of $\boldsymbol{i}_{\hat{d}q}$ and the sign of ω, and as $h \to \infty$, $K_{\omega 0} \to 1$.

$$K_{\omega 0} = \frac{g^2 + s\,g + (s^2 + \omega_0^2 + s\,g)\left(\frac{h}{s+h}\right)}{(s+g)^2 + \omega_0^2} \tag{33}$$

The bode plot of $K_{\omega 0}$ at various speeds is shown in the Fig. 9; unlike $K_{\theta 0}$, $K_{\omega 0}$ is strongly influenced by the derivative observer. At $h = 0$ in Fig. 9.a, the speed error is unobservable at high speeds as the gain is very small. Hence, the derivative observer is deemed essential for speed error estimation as in the Fig. 9.b which exhibits a low-pass filter behavior with a cut-off frequency at h.

A perturbation analysis is developed to validate the accuracy of position and speed error estimation. To this end, a sinusoidal disturbance is injected into the encoder position measurement as shown in Fig. 10 and the estimated error are juxtaposed against the reference errors.

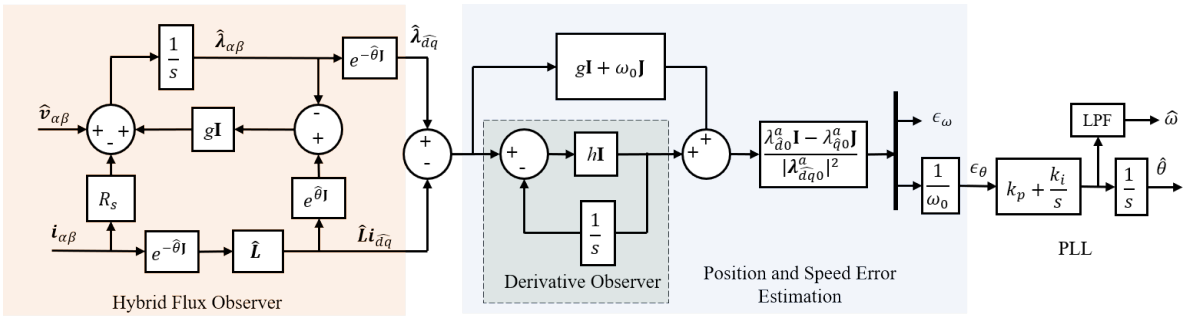

Fig. 6. Proposed speed and position observer, APPS: h is the bandwidth of derivative observer for the term $s\,(\hat{\boldsymbol{\lambda}}_{\hat{dq}} - \hat{\boldsymbol{L}}\,\boldsymbol{i}_{\hat{dq}})$

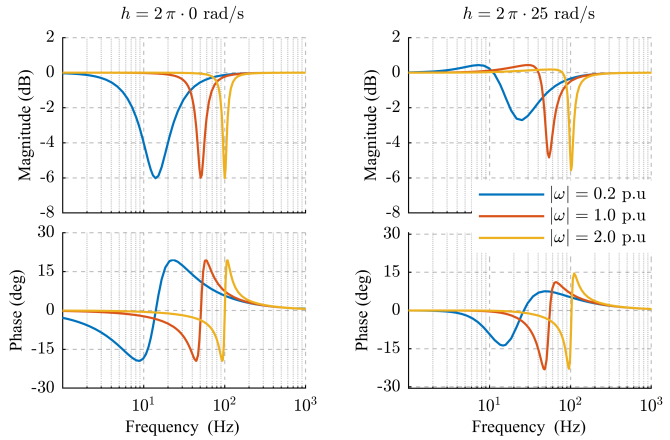

Fig. 7. Bode plot of $K_\theta(s) = \epsilon_\theta/\tilde{\theta}$ at $g = 2\pi \cdot 10$ rad/s exhibiting a band-stop filter like behavior: a) $h = 2\pi \cdot 0$ rad/s; b) $h = 2\pi \cdot 25$ rad/s

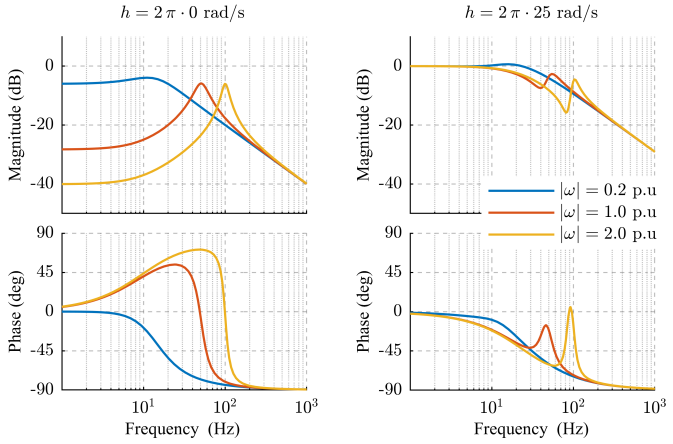

Fig. 9. Bode plot of $K_\omega(s) = \epsilon_\omega/\tilde{\omega}$ at $g = 2\pi \cdot 10$ rad/s exhibiting a low-pass filter like behavior: a) $h = 2\pi \cdot 0$ rad/s; b) $h = 2\pi \cdot 25$ rad/s

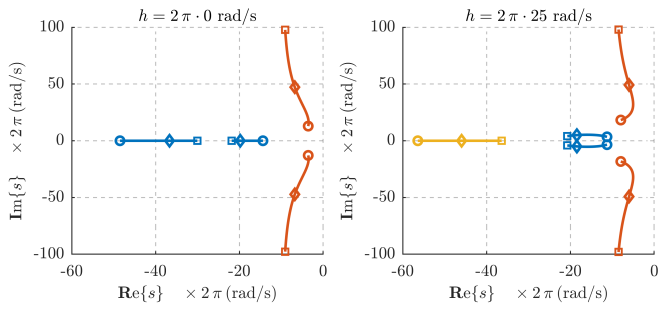

Fig. 8. Locus of poles of speed observer for $|\omega|$ = 0.2. . . 2 p.u: a) $h = 2\pi \cdot 0$ rad/s; b) $h = 2\pi \cdot 25$ rad/s. The circle, diamond and square represents the speeds 0.2 p.u, 1 p.u and 2 p.u respectively. The poles of PLL are in blue, flux observer in red and derivative observer in yellow; $g = 2\pi \cdot 10$ rad/s and the gains of PLL are tuned according to (34) with $\Omega_\omega = 2\pi \cdot 25$ rad/s.

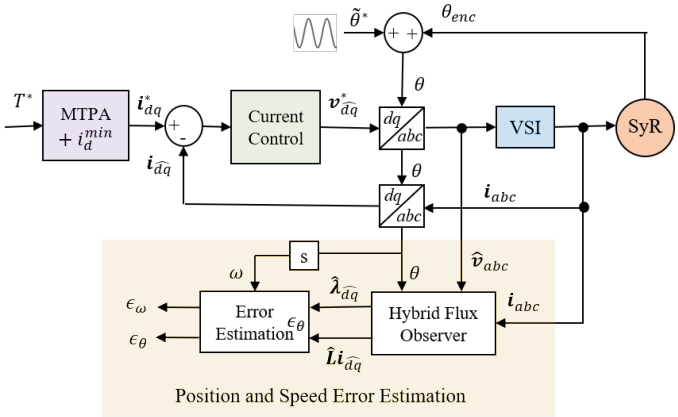

Fig. 10. Perturbation of encoder measurement to validate speed and position error estimation in APPS scheme

V. Experimental Results

The proposed sensorless scheme is validated experimentally on a 1 kW SyR motor on a dspace DS1103 control platform running at a sampling frequency of 10 kHz. A picture of the setup is shown in Fig. 11. The parameters of the SyR under test are tabulated in Table I.

The gains of the PLL are tuned for a critically damped response at $K_{\epsilon 0} = 1$ by placing the two poles at $s = -\Omega_\omega$:

$$k_p = 2\,\Omega_\omega \qquad k_i = \Omega_\omega^2 \tag{34}$$

The observer bandwidth $\Omega_\omega = 2\pi \cdot 25$ rad/s is chosen; the estimated speed is low-pass filtered at Ω_ω. The flux observer gain is set to $g = 2\pi \cdot 10$ rad/s. Unless otherwise mentioned, the derivative observer gain is set to $h = 2\pi \cdot 25$ rad/s.

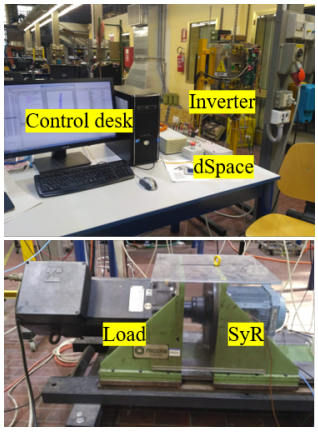

Fig. 11. Experimental Setup of 1 kW SyR motor under test on a dspace DS1103 control platform at a sampling frequency of 10 kHz.

TABLE I
MOTOR PARAMETERS

Parameters	Symbol	Values	Units
Rated Power	P_n	1	kW
Rated Voltage	V_n	340	V
Rated Speed	ω_n	1500	rpm
Rated Current	I_n	3.6	A
Rated Torque	T_n	7.1	Nm
Pole pairs	p	2	-
Stator Resistance	R_s	4.5	Ω
Shaft Inertia	J	0.04	kgm^2

The SyR motor is speed controlled while the load torque is imposed by an auxiliary drive. A minimum current in $i_d^{min} = 0.4$ p.u (2A) is imposed to saturate the q axis ribs at no-load.

A. Validation of Improved Inductance Model using Active Flux Method

To highlight the veracity of proposed improvements on inductance model, the active flux transfer function $K_{\epsilon 0}$ in (25) is simplified excluding the dynamics to (35) at $\omega = -g$;

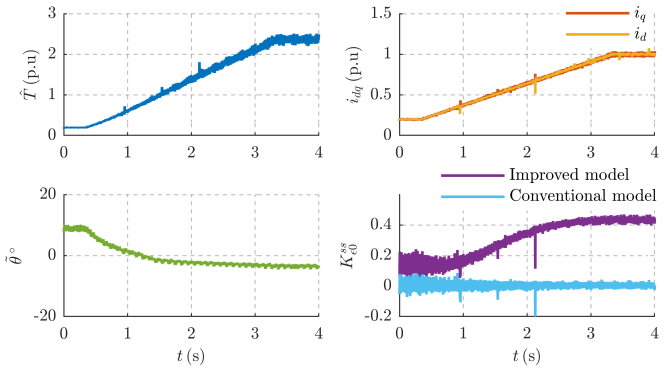

Fig. 12. Effect of improved inductance model on stability analysis. Operating conditions: $\omega = -g = -0.4$ p.u, current angle = 45° ($i_d = i_q$)

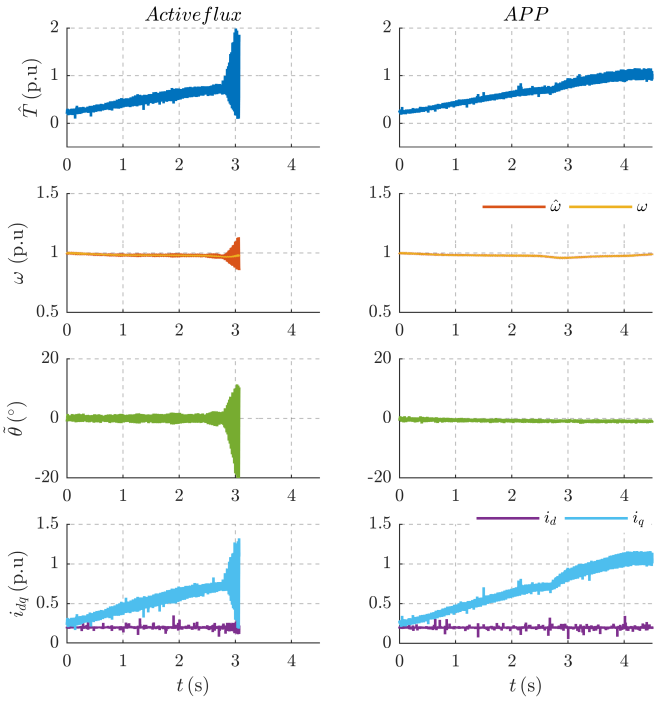

Fig. 13. Operation at high speeds motoring region for trajectory along MTPV at $\omega = 1$ p.u: a) Active flux approach; b) APP technique. Instability of active flux method occurs at $t = 2.75$ s.

the steady-state term $K_{\epsilon 0}^{ss}$ (scaling factor of speed observer bandwidth) is given by

$$K_{\epsilon 0}^{ss} = \frac{1}{(\hat{L}_d - \hat{L}_q)\, i_{\hat{d}0}} \cdot \frac{1}{2}\left(\lambda_{\hat{q}0}^{a} - \lambda_{\hat{d}0}^{a}\right) \tag{35}$$

For the conventional inductance model (using $\boldsymbol{\lambda}_{\hat{d}q0}^{a'}$ in (35)), the term $K_{\epsilon 0}^{ss} = 0$ at $i_d = i_q$ which implies an unobservable state. However, as shown in Fig. 12, it is a stable operating state as affirmed by using the improved inductance model, (17) in (35). The steady-state position error in Fig. 12 arises due to the low $K_{\epsilon 0}^{ss}$ that diminishes the strength of error signal ϵ_θ making it more susceptible to inverter non-idealities.

B. Stability Analysis: Active Flux Vs. APP

As illustrated in Fig. 5, instability of active flux approach is pronounced at high speeds motoring and low speeds braking regions.

1) Motoring: Fig. 13 shows the operation at $\omega = 1$ p.u along the MTPV trajectory with an imposed minimum $i_d^{min} = 0.2$ p.u. The active flux approach runs into instability well below the rated torque while the proposed APP technique alleviates the problem with negligible steady-state position error.

2) Braking: In the case of braking in Fig. 14 at $\omega = -0.2$ p.u along the MTPA trajectory, the active flux approach becomes unstable at T ≈ 0.5 p.u while the proposed APP technique is capable of tracking the torque reference.

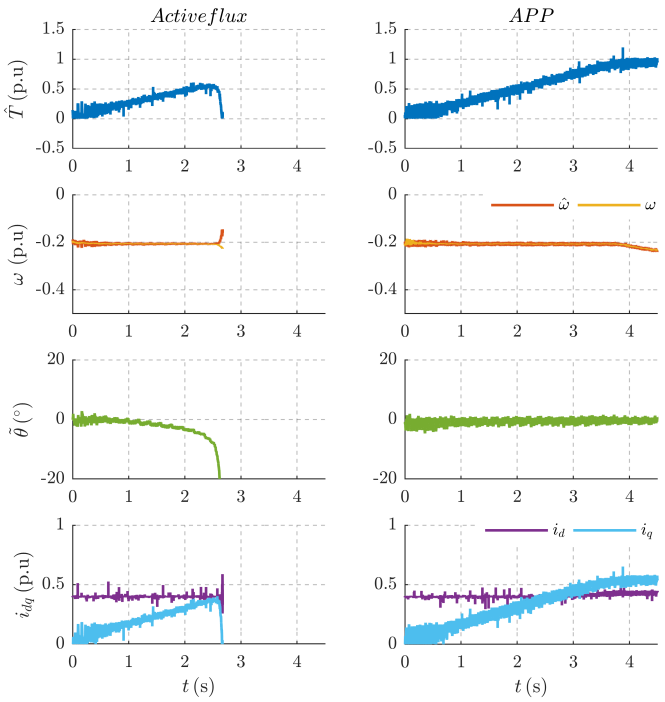

Fig. 14. Operation at low speeds braking region for trajectory along MTPA at $\omega = -0.2$ p.u: a) Active flux approach; b) APP technique. Instability of active flux method occurs at $t = 2.5$ s.

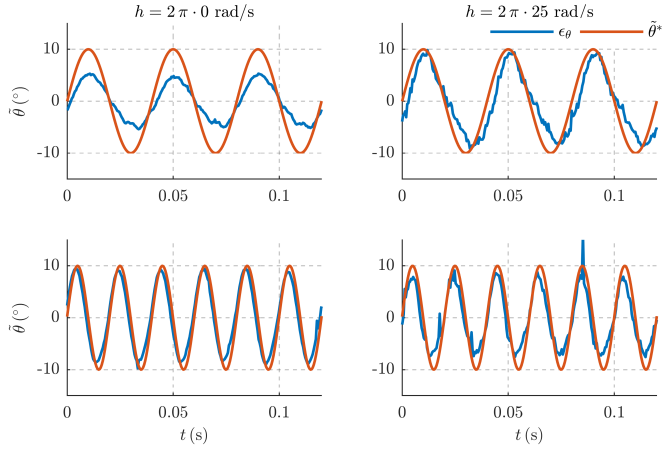

Fig. 15. Position error estimation of APPS under imposed sinusoidal perturbation of $\tilde{\theta}^* = 10° \sin(2\pi \cdot 25\,t)$ and $\tilde{\theta}^* = 10° \sin(2\pi \cdot 50\,t)$ (electrical) on encoder measurement: a) $h = 2\pi \cdot 0$ rad/s; b) $h = 2\pi \cdot 25$ rad/s . Operating conditions: T = 0.5 p.u and ω = 0.5 p.u

C. Perturbation Analysis

Note that the PLL is disabled for this test as the system is no longer sensorless; moreover, the SyR is in torque control operation with a constant speed imposed by the auxiliary drive.

Fig. 15 shows the position error in APPS technique when a sinusoidal perturbation of $\tilde{\theta}^* = 10° \sin(2\pi \cdot 25\,t)$ and $\tilde{\theta}^* = 10° \sin(2\pi \cdot 50\,t)$ are imposed on the encoder position measurement. The band-stop behavior of K_θ in Fig. 7 at $\omega = 0.5$ p.u (25 Hz) is more visible for $h = 2\pi \cdot 0$ rad/s

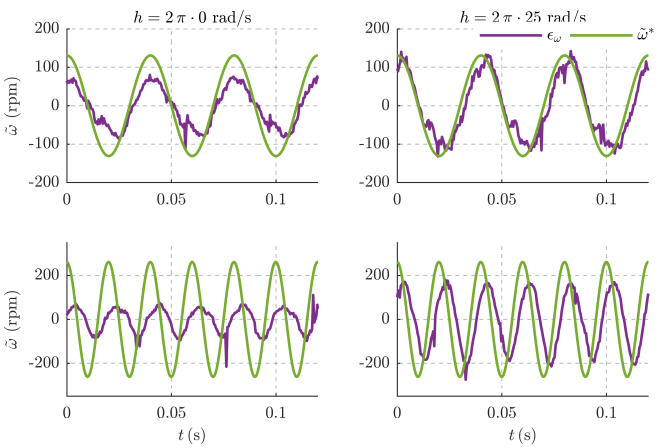

Fig. 16. Speed error estimation of APPS under imposed sinusoidal perturbation of $\tilde{\theta}^* = 10° \sin(2\pi \cdot 25\,t)$ and $\tilde{\theta}^* = 10° \sin(2\pi \cdot 50\,t)$ (electrical) on encoder measurement: a) $h = 2\pi \cdot 0$ rad/s; b) $h = 2\pi \cdot 25$ rad/s. Operating conditions: T = 0.5 p.u and ω = 0.5 p.u

where the position error signal ϵ_θ tracks the $\tilde{\theta}^*$ oscillations at 50 Hz while it falters at the notch frequency of 25 Hz.

The bode plot of K_ω in Fig. 9 dictates a low-pass behavior with cut-off frequency at h; accordingly, in Fig. 16, speed error signal ϵ_ω at $h = 2\pi \cdot 25$ rad/s tracks accurately the $\tilde{\omega}^*$ oscillations at 25 Hz but falters at 50 Hz. As expected, the inclusion of derivative observer improves the tracking of speed and position errors.

D. Transient performance

The performance of APP technique with/without the derivative observer during transients is analyzed with step change in load torque and reference speed in Fig. 17 and Fig. 18 respectively. In either case, a negligible transient error in position is observed. Moreover, the exclusion of derivative observer in Fig. 17.a and Fig. 18.a makes little difference as supported by bode plot of K_θ in Fig. 7.

VI. Conclusion

This paper presents a framework for the design and analysis of position observers for SyR machines in sensorless applications. An improved inductance model is developed to account for the position error induced variations. The well-known active flux based position observer is subjected to analysis to reveal instability at high speeds flux-weakening and low speeds braking regions.

A new observer is developed with an adaptive position error projection vector, APP, to alleviate the stability problems. Furthermore, the APP technique can be augmented with an additional projection vector to obtain APPS that is capable of estimating speed error signal independently by having speer error projection vector orthogonal to the position error projection vector. A derivative observer is introduced which is deemed essential for speed error estimation; however, could be optional if only position error is sufficient.

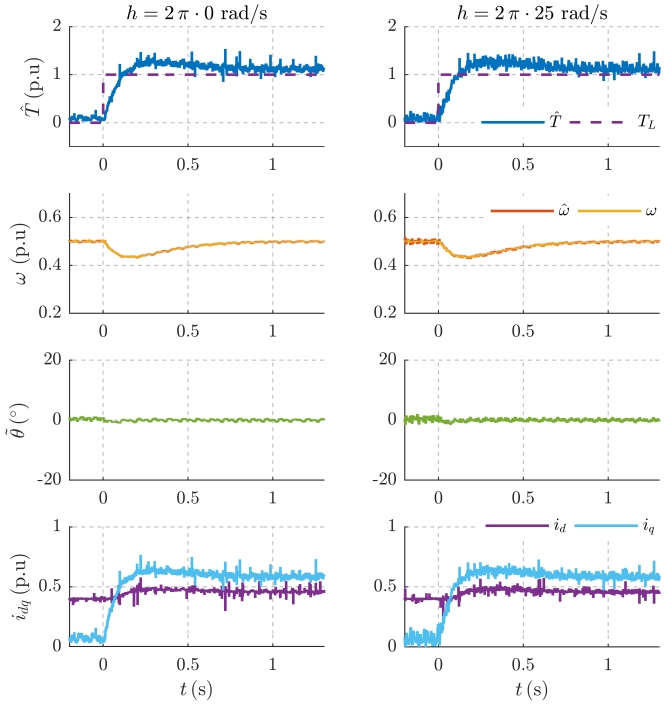

Fig. 17. Transient performance of the APP technique for a rated step change in load torque, $T_L = 0 \rightarrow 1$ p.u, at $\omega = 0.5$ p.u: a) $h = 2\,\pi \cdot 0$ rad/s; b) $h = 2\,\pi \cdot 25$ rad/s

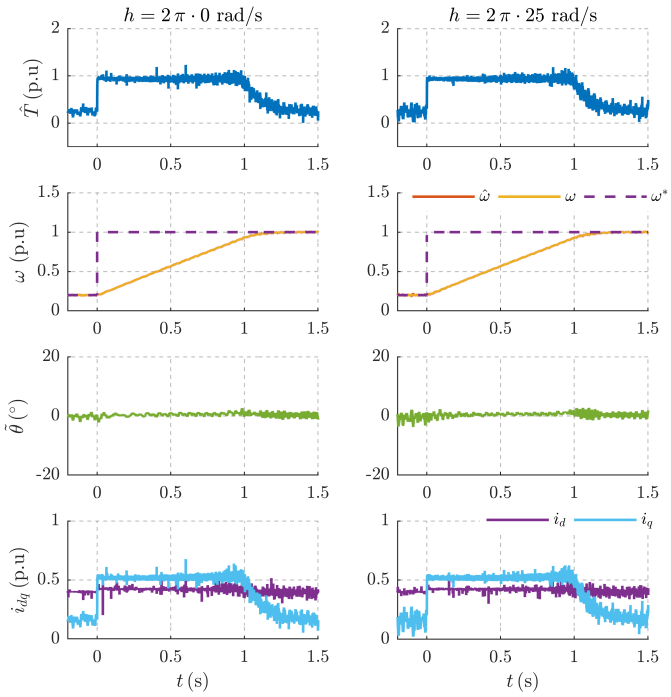

Fig. 18. Transient performance of the APP technique for a step change in speed reference, $\omega = 0.2 \rightarrow 1$ p.u, at a load torque $T_L = 0.15$ p.u: a) $h = 2\,\pi \cdot 0$ rad/s; b) $h = 2\,\pi \cdot 25$ rad/s

The stability concerns with active flux method, transient and steady-state performance of the APP technique along with the perturbation analysis of APPS for speed error estimation are experimentally evaluated on a 1 kW SyM motor test bench.

REFERENCES

[1] C. Hwang, Y. Lee, and S. K. Sul, "Analysis on Position Estimation Error in Position-Sensorless Operation of IPMSM Using Pulsating Square Wave Signal Injection," *IEEE Transactions on Industry Applications*, p. 1, 2018.

[2] E. Capecchi, P. Guglielmi, M. Pastorelli, and A. Vagati, "Position-sensorless control of the transverse-laminated synchronous reluctance motor," *IEEE Transactions on Industry Applications*, vol. 37, no. 6, pp. 1768–1776, 2001.

[3] A. Varatharajan, P. Pescetto, and G. Pellegrino, "Injectionless Sensorless Control of Synchronous Reluctance Machine for Zero to Low Speeds Region," in *2018 IEEE 9th International Symposium on Sensorless Control for Electrical Drives (SLED)*, 2018, pp. 72–77.

[4] F. Briz and M. W. Degner, "Rotor Position Estimation," *IEEE Industrial Electronics Magazine*, vol. 5, no. 2, pp. 24–36, 2011.

[5] A. Yousefi-Talouki, P. Pescetto, G. Pellegrino, and I. Boldea, "Combined Active Flux and High Frequency Injection Methods for Sensorless Direct Flux Vector Control of Synchronous Reluctance Machines," p. 1, 2017.

[6] S. C. Agarlita, I. Boldea, and F. Blaabjerg, "High-frequency-injection-assisted 'active-flux'-based sensorless vector control of reluctance synchronous motors, with experiments from zero speed," *IEEE Transactions on Industry Applications*, vol. 48, no. 6, pp. 1931–1939, 2012.

[7] F. J. Barnard, W. T. Villet, and M. J. Kamper, "Hybrid Active-Flux and Arbitrary Injection Position Sensorless Control of Reluctance Synchronous Machines," *IEEE Transactions on Industry Applications*, vol. 51, no. 5, pp. 3899–3906, 2015.

[8] M. Hinkkanen, S. E. Saarakkala, H. A. A. Awan, E. Molsa, and T. Tuovinen, "Observers for Sensorless Synchronous Motor Drives: Framework for Design and Analysis," *IEEE Transactions on Industry Applications*, p. 1, 2018.

[9] Y. Lee and S. K. Sul, "Model-Based Sensorless Control of an IPMSM With Enhanced Robustness Against Load Disturbances Based on Position and Speed Estimator Using a Speed Error," *IEEE Transactions on Industry Applications*, vol. 54, no. 2, pp. 1448–1459, 2018.